Organic Electronics 71 (2019) 175–184

Contents lists available at ScienceDirect

Organic Electronics

journal homepage: www.elsevier.com/locate/orgel

Plasmonic hole-transport-layer enabled self-powered hybrid perovskite photodetector using a modified perovskite deposition method in ambient air

Joydip Ghosh[a], Gayatri Natu[b], P.K. Giri[a,b,*]

[a] Department of Physics, Indian Institute of Technology Guwahati, Guwahati, 781039, India
[b] Centre for Nanotechnology, Indian Institute of Technology Guwahati, Guwahati, 781039, India

ARTICLE INFO

Keywords:
Plasmonic perovskite photodetector
Self-biased photodetector
Kelvin probe force microscopy
Fast photoresponse

ABSTRACT

Herein, we report on an air-processed high performance self-powered hybrid perovskite (Pe) photodetector with plasmonic Silver nanoparticle (Ag NP) embedded hole-transport-layer (HTL), without the use of any electron-transporting layer (ETL). It is demonstrated that in the absence of ETL in the device, the Ag NPs embedded PEDOT:PSS HTL improves the photodetection performance significantly. We used a novel N_2 gas assisted fast crystallization method for the deposition of perovskite film in ambient condition to form uniform Pe layer as compared to the nonuniform film obtained in conventional deposition method. The Pe film on Ag NPs embedded PEDOT:PSS layer shows enhanced optical absorption in the UV–visible region due to the plasmonic absorption by the Ag NPs. At zero bias, the ETL-free Ag NPs-Pe hybrid device shows ~45% enhanced responsivity and ~3 times faster photoresponse compared to the pristine device. The enhancements in the performance of hybrid photodetector are attributed to plasmon-enhanced optical absorption and hot electron generation, as well as improvement in charge extraction and transport by Ag NPs, which are corroborated by steady-state and time-resolved photoluminescence measurements. Impedance analysis of the devices shows the reduced carrier transfer resistance of the hybrid device, which results in superior transport of photo-generated charge carriers. Direct evidence for the increase in the work function by ~47 meV for Ag NPs doped PEDOT:PSS film is provided from the Kelvin probe force microscopy analysis. This increase in work function enables favorable band alignment with reduced energy barrier and a superior carrier transport resulting in improved photodetection performance for the hybrid device. Our results are significant for the development of high-performance, low-cost, ETL free plasmonic perovskite photodetectors for futuristic applications.

1. Introduction

Organic-inorganic hybrid perovskites, especially methylammonium lead iodide ($CH_3NH_3PbI_3$), have drawn remarkable research attention over the past few years for their extraordinary performance in solar cells and optoelectronic devices with the advantages of broad absorption in UV–visible region, low cost and low-temperature processing, long exciton diffusion lengths, and superior charge transport [1–4]. Besides the outstanding power conversion efficiencies (> 23%) of Perovskite (Pe) solar cells [1], the impressive photoelectric conversion of solution-processed Pe has prompted for their applications in other semiconductor-based devices, such as light-emitting diodes (LEDs), laser and photodetectors [5–11].

A photodetector is a device that captures the light signal and converts it into an electrical signal. The ultrasensitive photodetection is important in a wide range of fields, such as optical communication, environmental monitoring, biomedical imaging, security, fire detection, night-vision, motion detection etc. [5,8,11] The key-of-merit parameters of a photodetector are operating voltage, responsivity (R), detectivity (D*), linear dynamic range (LDR) and response speed etc. [6,12–14] In most commercial photodetectors [15,16], an external bias is essential to achieve the specified performance. Numerous types of semiconducting materials, such as Si, ZnO, GaN etc., have been used in photodetectors, although there are certain limitations due to the complicated fabrication process, high power consumption, high cost and bulkiness of the photodetectors [17,18]. In contrast, the fabrication of Pe based photodetector is much simpler due to its low-cost solution processable fabrication [6,7,19–24]. Perovskite photodetector with planar and mesoporous “solar cell structure” has recently been reported, which shows excellent performances [6,25]. Bao et al. showed highly flexible self-powered perovskite photodetectors with gold nanowire networks with responsivity 321 mA/W and response speed of

* Corresponding author. Department of Physics, Indian Institute of Technology Guwahati, Guwahati, 781039, India.
E-mail address: giri@iitg.ac.in (P.K. Giri).

https://doi.org/10.1016/j.orgel.2019.05.021
Received 19 March 2019; Received in revised form 27 April 2019; Accepted 11 May 2019
Available online 14 May 2019
1566-1199/

4 μs. [6]. Sutherland et al. reported self-powered perovskite photodetector by exploiting interface engineering, which shows 1 μs temporal response and responsivity of 0.4 AW^{-1} [26]. Dou et al. reported solution processed perovskite photodetector with large detectivity approaching 10^{14} Jones, a linear dynamic range over 100 decibels and a fast photoresponse with 3-dB bandwidth up to 3 MHz [8]. In these types of p-i-n or n-i-p photodetectors, one hole transporting layer (HTL) and one electron transporting layer (ETL) are used to separate and transport of photogenerated electrons and holes, while Pe layer acts as a light absorbing active material. Interestingly, these photodetectors can operate without any external bias, though stability and cost are the principal issues for these devices, as different organic HTL and ETL accelerate the degradation of the device [27]. Pe photodetectors with 2D materials (e.g. graphene, MoS_2) and without ETL-HTL layer have also been reported, though they require high applied bias for the operation [7,20,28]. However, self-powered devices are highly desirable for most cutting-edge applications [19,28]. Another important issue of perovskite photodetector is the poor device performance when fabricated under ambient condition. The perovskite film processed in ambient air is often highly nonuniform and rough, which results in poor device performance. Thus, it is imperative to study Pe photodetectors without any charge transporting layer or an external bias with modified perovskite deposition method and processed in ambient air.

Use of plasmonic metal nanoparticles (NPs) in solar cells and optoelectronic devices dramatically improves the device performance. Metal NPs under photon illumination can give rise to localized surface plasmon resonance (LSPR), which induces strong photon scattering and absorption. Thus, the photon absorption of the surrounding material can be improved via both the increase by the plasmonic scattering and the near-field enhancement induced excitation effects [16,29]. Plasmonic metal NPs also lead to better charge separation and transport. Very recently, Wang et al. showed Au nanorods-Pe hybrid photodetector with high responsivity and low operating voltage, while Du et al. reported plasmonic functionalized photodetector using Au nanosquares array [16,30].

Herein, we report on the enhanced performance of an ETL-free self-powered Pe photodetector by embedding plasmonic Ag NPs in the HTL layer. Ag NPs were synthesized by well-known citrate reduction method and different concentrations of Ag NPs dispersed in water were added to PEDOT:PSS HTL and deposited by spin coating on a patterned FTO/glass substrate. As 20 vol% Ag NPs added with PEDOT:PSS (Ag20) shows the optimum result in the device performance, detailed comparative characterizations were performed with pure PEDOT:PSS HTL devices (Ag0) and Ag20 devices. For the deposition of Pe active layer, we used a novel N_2 gas assisted fast crystallization method to form uniform Pe layer in ambient air (with high relative humidity). The conventional deposition method in ambient condition produces rough and nonuniform perovskite film, which results in poor device performance and stability. The x-ray diffraction spectra confirm the desired tetragonal phase of the Pe, while the UV–visible absorption spectra reveal that with Ag NPs the absorbance is enhanced in the near UV–visible region due to the plasmon resonance absorption by Ag NPs. Photoluminescence (PL) and time-resolved PL (TRPL) results confirm the enhanced charge separation and efficient transport by the PEDOT:PSS film with Ag NPs. The hybrid photodetector (with Ag NPs) shows high responsivity and the detectivity along with faster photoresponse than the pristine (without Ag NPs) one. Impedance analysis of the devices shows the reduced carrier transfer resistance of the hybrid device, which results in superior transport of photogenerated charge carriers. The Kelvin probe force microscopy (KPFM) was used to evaluate the change of the surface potential of PEDOT:PSS layer with the addition of Ag NPs, which unravels the mechanism of enhanced performance of the hybrid device. All the fabrication and measurements were done in an open atmosphere with high humidity (60%).

2. Experimental details

2.1. Materials

All reagents were used as received without further purification. The purchased reagents are methylamine solution (CH_3NH_3, 33 wt % in absolute ethanol, Sigma Aldrich), lead(II) iodide (PbI_2, 99%, Sigma Aldrich), hydroiodic acid (HI, 57 wt % in water, Sigma Aldrich), N,N-dimethyl formamide (DMF, > 99%, Sigma Aldrich), diethyl ether (> 99%, Merck), $AgNO_3$ (> 99.5%, Merck) PEDOT:PSS (1.3 wt % dispersion in H_2O, Sigma Aldrich), PCBM (> 99.5%, Sigma Aldrich), trisodium citrate (99%, Alfa Aesar).

2.2. Synthesis of CH_3NH_3I

CH_3NH_3I was synthesized by reaction of 24 mL methylamine solution (33 wt % in ethanol), 10 mL of hydroiodic acid (HI, 57 wt %) and 100 mL ethanol in 250 mL round bottom flask at 0 °C for 2 h with stirring at 400 rpm [31]. The precipitate was collected by evaporating the solvent at 60 °C for 3 h. Next precipitate was washed 3 times with diethyl ether and finally collected after recrystallization. Then CH_3NH_3I crystals were dried overnight at 60 °C in a vacuum oven.

2.3. Synthesis of Ag nanoparticles

Ag NPs was synthesized freshly by chemical reduction method using trisodium citrate solution as a reducing agent. First, a solution of 50 mL of 4 mM $AgNO_3$ in double distilled water was prepared and heated to its boiling point using the hot plate and magnetic stirrer. Next 10 mL of 2% trisodium citrate was added dropwise to the solution. During this process, the solution was stirred vigorously and heated until its color became yellowish brown. Next, it was removed from the heating element and stirred until it cooled down to room temperature. The NPs were collected by centrifugation at 10000 rpm and redispersed in water via sonicating for 15 min.

2.4. Device fabrication

The schematic of the fabrication process and device configuration of the hybrid photodetector is shown in Fig. 1. The fluorine doped tin oxide (FTO) coated glass substrates with a sheet resistance of 7 Ω/sq were patterned by using zinc powder and HCl solution, then cleaned sequentially with deionized water, acetone, isopropanol and ethanol using an ultrasonic cleaner for 20 min respectively, and dried in N_2 gas flow. The FTO substrates were treated by UV ozone cleaner for 15 min. 10, 20 and 30 vol% Ag NPs solution is added with PEDOT:PSS solution and homogenized by ultrasonication, which are named as Ag10, Ag20, and Ag30, respectively. Note that the bare PEDOT:PSS without Ag NPs is named as Ag0. PEDOT:PSS solution was spin-coated at 4000 rpm for 30 s on the cleaned patterned FTO glass, followed by annealing at 125 °C for 25 min. To prepare the Pe precursor solution with concentration 1.35 M, 0.212 g of methylammonium iodide (CH_3NH_3I) and 0.62 g of lead iodide (PbI_2) are dissolved in a solvent of 1 mL N,*N*-dimethylformamide (DMF) and heated for 1 h to form a yellow color transparent solution. We found that conventionally followed spin coating in the ambient atmosphere produces rough and nonuniform Pe film, and the multiple drop-casting using anti-solvent results in nonuniform Pe layer and poor reproducibility of the device. To form a uniform Pe layer, we used dry N_2 gas flow during the spin coating for the rapid crystallization and uniformity of the film. Perovskite precursor solution with a concentration of 1.35 M in DMF was spin-coated on PEDOT: PSS layer at 3500 rpm for 30 s. The samples were then dried at 90 °C for 10 min after deposition to produce a dark brown dense $CH_3NH_3PbI_3$ film. For the electron transporting layer (ETL) free devices, finally, 100 nm aluminum electrodes were deposited by thermal evaporation under high vacuum. For devices with ETL, a 20 mg/mL

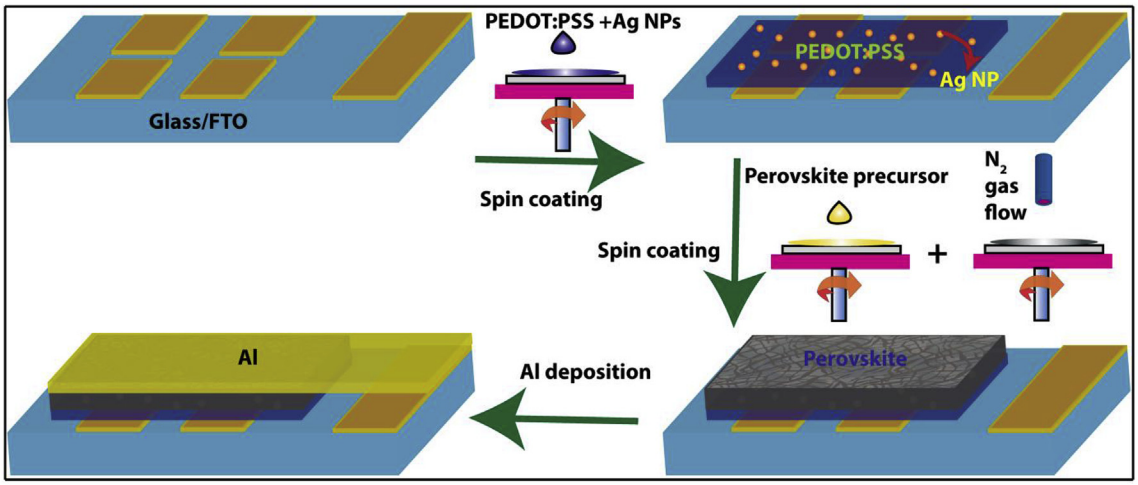

Fig. 1. Schematic of the device fabrication steps of plasmonic perovskite photodetector.

solution of PCBM was prepared in chlorobenzene and deposited via spin coating at 1000 rpm for 30 s. Then aluminum electrodes were deposited by thermal evaporation. All the fabrication process was carried out in an open-air atmosphere with high humidity (60%).

2.5. Characterization techniques

The morphology and elemental compositions of Pe and PEDOT: PSS film were characterized using a field emission scanning electron microscope (FESEM, Sigma, Zeiss) equipped with an energy dispersive x-ray (EDX) spectrometer. The high magnification image of Ag NPs was studied using a transmission electron microscope (TEM) (JEOL-JEM 2010) operated at 200 kV. Bruker Innova atomic force microscope (AFM) was used in tapping mode for examination of the topography of Pe films. Further, Bruker EFM (electrostatic force microscopy) toolkit with probe carrier and sample holder enabled with biasing leads was utilized in the Innova AFM for KPFM, i.e. for visualization of work function at the surface of the HTL film. The EFM uses a combination of tapping mode, lift mode and a conductive AFM tip to provide information pertaining to the electric field above a conductive sample. For structural characterizations of perovskite film, X-ray diffractometer (XRD) (Rigaku RINT 2500 TRAX − III, Cu Kα radiation) was used for different samples. UV–vis absorbance spectra of the samples were measured using a commercial spectrophotometer (PerkinElmer, Lamda 950). The steady-state photoluminescence (PL) spectrum of different samples was recorded using a 405 nm diode laser excitation with the help of a commercial fluorimeter (Horiba Jobin Yvon, Fluoromax-4). Time-resolved PL (TRPL) measurements were performed using a 405 nm pulsed laser excitation, with an instrument time response of < 50 ps (LifeSpecII, Edinburgh Instruments). Different characterizations were performed soon after the fabrication to avoid the degradation of perovskite film. The I–V characteristics and the photoelectric response curves of the photodetector were measured using a homemade setup using a Xenon lamp (Newport, USA) with a manual monochromator (Newport, USA), a chopper (Stanford Research Systems, USA) and a source meter (Keithley 2400, Germany). All the measurements were performed under ambient conditions with relatively high humidity.

3. Results and discussion

The schematic of the fabrication process and device configuration of the hybrid photodetector is shown in Fig. 1. Fig. 2(a) depicts the FESEM image of Pe layer fabricated by N_2 gas assisted crystallization method which reveals the compact grains and full coverage Pe film on FTO/Ag20. Note that the conventional deposition method in ambient air (with high humidity) results in highly nonuniform and rough film, as revealed from the FESEM imaging shown in Fig. S1(a) (supporting information). Fig. 2(b) shows the cross-sectional FESEM image of the device. The thickness of the perovskite active layer is ~590 nm. Fig. 2(c) shows the AFM image of Pe film, which clearly shows the large grains of as-deposited Pe layer. The rms roughness of the film is ~64 nm and grain sizes are in the range ~a few 100 nm to 2 μm. Fig. S2(a,b) (supporting information) shows the FESEM images of PEDOT: PSS film without and with Ag NPs, respectively, while Fig. S2(c,d) shows the EDX spectra of PEDOT: PSS film without and with Ag NPs. The EDX spectrum confirms the presence of Ag in Ag20 film.

Size, morphology and crystal structure of as-grown Ag NPs are studied using TEM/HRTEM lattice imaging and the results are shown in Fig. 2 (d,e). The lattice spacing 0.24 nm corresponds to (111) plane of silver as shown in Fig. 2(e) [32]. The inset of Fig. 2(d) shows the size distribution Ag NPs. The size of the Ag NPs is in the range 5–14 nm with a mean size ~11 nm (Fig. 2(d)). The absorption spectrum of as-grown Ag NPs dispersed in water shows a strong peak at ~432 nm corresponding to the characteristic plasmonic absorption of Ag NPs as shown in Fig. 2(f) which helps in better light harvesting in the plasmonic Pe device (discussed later).

The phase and crystalline quality of Pe film were confirmed by X-ray diffraction (XRD) analysis. XRD patterns of Pe film on glass, FTO/Ag0 and FTO/Ag20 shown in Fig. 3(a) confirm the crystalline phase of the $CH_3NH_3PbI_3$, consistent with the literature [3]. All the samples show nearly identical XRD pattern and it indicates that the structural ordering and preferential orientation of the crystallites relative to the substrate are retained in all the films. The strong diffraction peaks at 2θ equal to 14.16°, 20.04°, 23.55°, 24.57°, 28.50°, 31.92°, 35.04°, 40.56°, 43.11°, and 50.25° can be assigned to (110), (112), (211), (202), (220), (310), (312), (224), (314) and (404) crystal planes, which indicate tetragonal structure of $CH_3NH_3PbI_3$ [3]. The peaks marked with the symbol '♦' are arising from the FTO substrate.

The optical absorption spectra of the $CH_3NH_3PbI_3$ Pe film on Ag0 and Ag20 are shown in Fig. 3(b). The Pe film exhibits a wide spectral absorption in the range 300–800 nm with a high absorption value. This gives rise to the high photo-responsivity of the photodetector over a broad spectral range (discussed later). Note that the Pe film on Ag20 shows enhanced absorption in the region 300–550 nm as compared to of Ag0. This is due to the plasmonic absorption by the Ag NPs, peaked at 432 nm as shown in Fig. 2(f). The absorption spectra of bare PEDOT:PSS film and PEDOT:PSS film with Ag NPs are shown in Fig. S3 (supporting information). Both the films show a very low absorbance in the wavelength region 300 nm–800 nm due to the high transmittance,

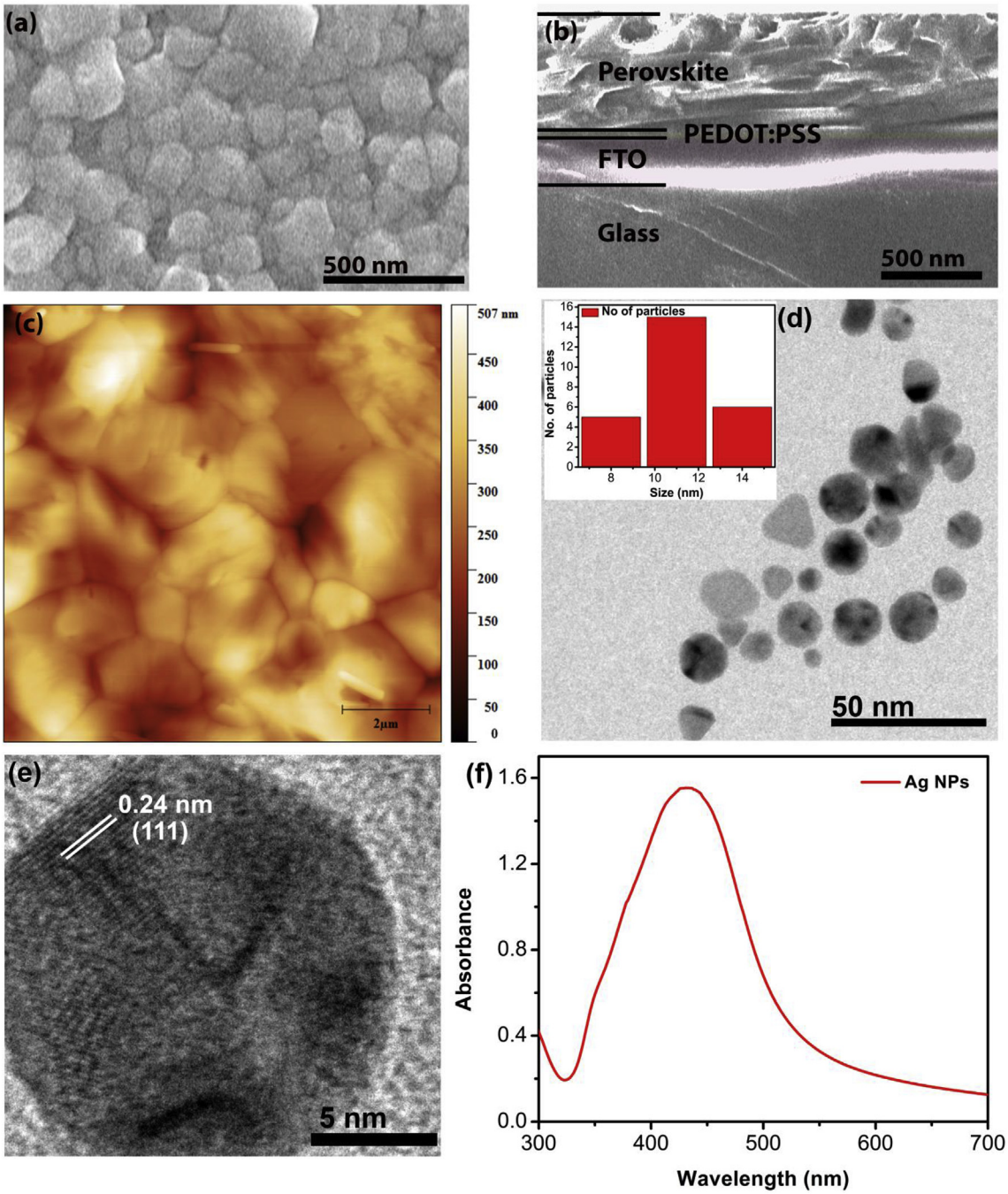

Fig. 2. (a) FESEM image of perovskite film on FTO/Ag20 layer. (b) Cross-sectional FESEM image of the device which shows the thickness of the different layers. (c) AFM image of perovskite film on FTO/Ag20 layer. (d) The TEM image of Ag NPs, the inset shows the corresponding size distribution of Ag NPs. (e) HRTEM lattice fringe of single Ag NP. (f) The UV–visible absorption spectrum of bare Ag NPs dispersed in water.

which is essential to photoexcite the Pe active layer. Interestingly with the Ag NPs, the absorbance of Ag20 film in the wavelength region 300–600 nm is marginally higher than Ag0 film. This is due to the plasmonic absorption by the Ag NPs in the film. In presence of the perovskite layer, the difference in absorbance is more prominent due to the multiple reflections at the interfaces.

To study the effect of Ag NPs on charge carrier dynamics, steady-state PL and TRPL measurements were carried out. The comparison of the PL spectra of the Pe film on FTO, Ag0, and Ag20 are shown in Fig. 3(c). A PL peak centered at ~779 nm for each sample corresponds to the photoemission peak for $CH_3NH_3PbI_3$ Pe due to the band to band transition [3]. Note that for films on Ag0 and Ag20, the PL intensity was quenched to 50.1% and 31.4% of the peak intensity of Pe film on FTO substrate. The PL of the Pe film on PEDOT:PSS layer was quenched due to the transfer of photogenerated charges from Pe to PEDOT:PSS layer, which decreases the radiative recombination. Further, with the introduction of Ag NPs, PL quenching was observed, indicating that the photo-excited carriers in Pe layer possibly transfer to Ag NPs by reducing the charge recombination and it is beneficial for the photodetection [16]. The charge transfer process is further ascertained from the TRPL analysis. Fig. 3(d) shows a comparison of the TRPL decay profiles of Pe film on FTO, Ag0, and Ag20 monitored at the PL peak center. TRPL data in each case was fitted by a bi-exponential decay function as [28].

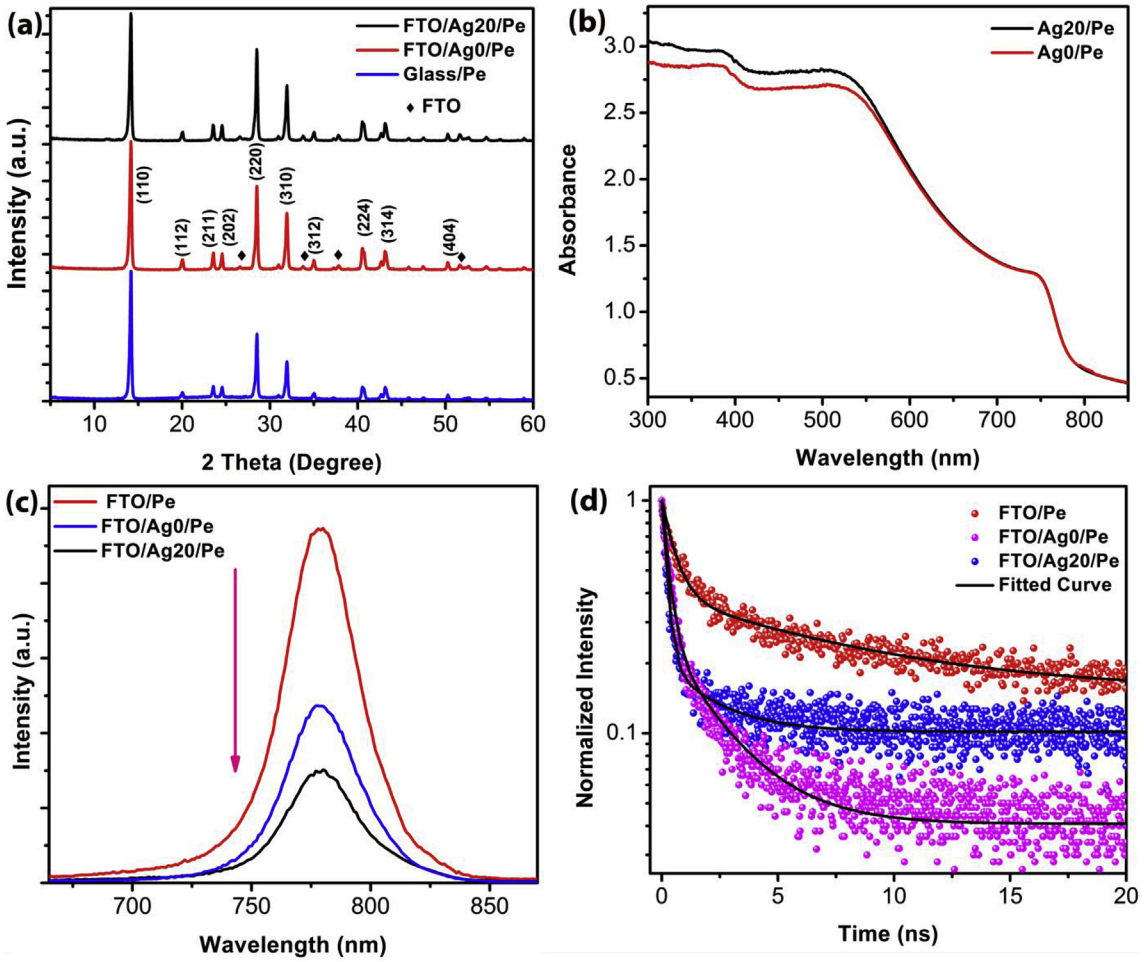

Fig. 3. Comparison of (a) XRD patterns, (b) absorbance spectra (c) steady-state PL spectra, (d) Time-resolved PL decay profiles of perovskite films on glass, FTO/Ag0, and FTO/Ag20. The symbols represent the experimental data and solid lines represent the fitted data in (d).

$$A(t) = A_1 \exp\left(-\frac{t}{\tau_1}\right) + A_2 \exp\left(-\frac{t}{\tau_2}\right), \quad (1)$$

where A_1 and A_2 are the amplitudes and τ_1 and τ_2 are the time constants of the TRPL decay, respectively. The average lifetimes (τ_{ave}) was estimated using the relation [28].

$$\tau_{ave} = (A_1\tau_1^2 + A_2\tau_2^2)/(A_1 + A_2) \quad (2)$$

The τ_{ave} are found to be 6.84 ns, 1.67 ns and 1.30 ns for Pe film on FTO, Ag0 and Ag20, respectively. The details of the time constants and amplitudes of different samples are tabulated in Table S1 (supporting information). The shortening of time constants indicates a faster charge transfer between the Pe and the PEDOT:PSS layer, resulting in an improved carrier separation from the Pe layer [16,33]. Note that the TRPL decay lifetime of Pe film on Ag20 is further decreased from than of Ag0, which confirms the better transfer of photogenerated carriers in Ag20.

Fig. S4(a) (supporting information) shows the comparison of XRD pattern of perovskite film on glass deposited by conventional deposition and N_2 gas assisted fast crystallization method in ambient air. Interestingly, the intensity of (110) XRD peak of Pe film made by the modified deposition method is enhanced ~4.9 times compared to the conventional deposition method. This may be due to the higher crystallinity and the full coverage of Pe film deposited by our modified deposition method. Further, PL spectra were measured for both the films. Fig. S4(b) (supporting information) depicts the PL spectra of Pe film fabricated on FTO/glass by conventional and the modified deposition method. The enhanced PL peak intensity of Pe film by the modified deposition method also confirms the better crystallinity and full coverage of the film.

To assess the performance of the photodetectors, we investigated the photocurrent (PC) switching, responsivity, and detectivity of the Pe photodetectors. It is significant to note that all the measurements were conducted at room temperature under ambient conditions with high humidity. The PC response and sustainability of pristine and hybrid devices were measured with repeated on/off switching cycles under illumination intensity 1.1 mW/cm^2 at zero bias. Fig. 4(a) shows the time-dependent PC response curves under zero bias with on/off intervals of 5 s with 400 nm incident light. From Fig. 4(a), it is clear that with the incorporation of Ag NPs in PEDOT:PSS layer, the PC of the hybrid device increased significantly as compared to that without the Ag NPs. The photocurrents for the devices with Ag0, Ag10, Ag20, Ag30 are 7.54, 8.83, 11.13 and 9.68 μA, respectively. Note that the PC first increased as a function of Ag NP concentration and showed the highest value for Ag20 case and then decreased for Ag30. This may be due to the structural inhomogeneity of the HTL induced by high concentration of Ag NPs that decreases the overall carrier transport through the layer by causing charge carrier scattering. Thus, the Ag20 device shows optimum performance. We, therefore, focused on the device with Ag20 for the HTL, and further investigations were made with comparative analysis of Ag0 and Ag20 devices. We have further quantified the photoresponse speed of growth and decay of PC of Ag0 and Ag20 devices [34]. Fig. 4(b) and (c) shows the enlarged view of a single cycle photoresponse of Ag20 and Ag0 devices, respectively. The rise time (τ_r) and decay time (τ_d) of PC can be defined as the time to transition between the minimum current to the 90% of the maximum value, and from the

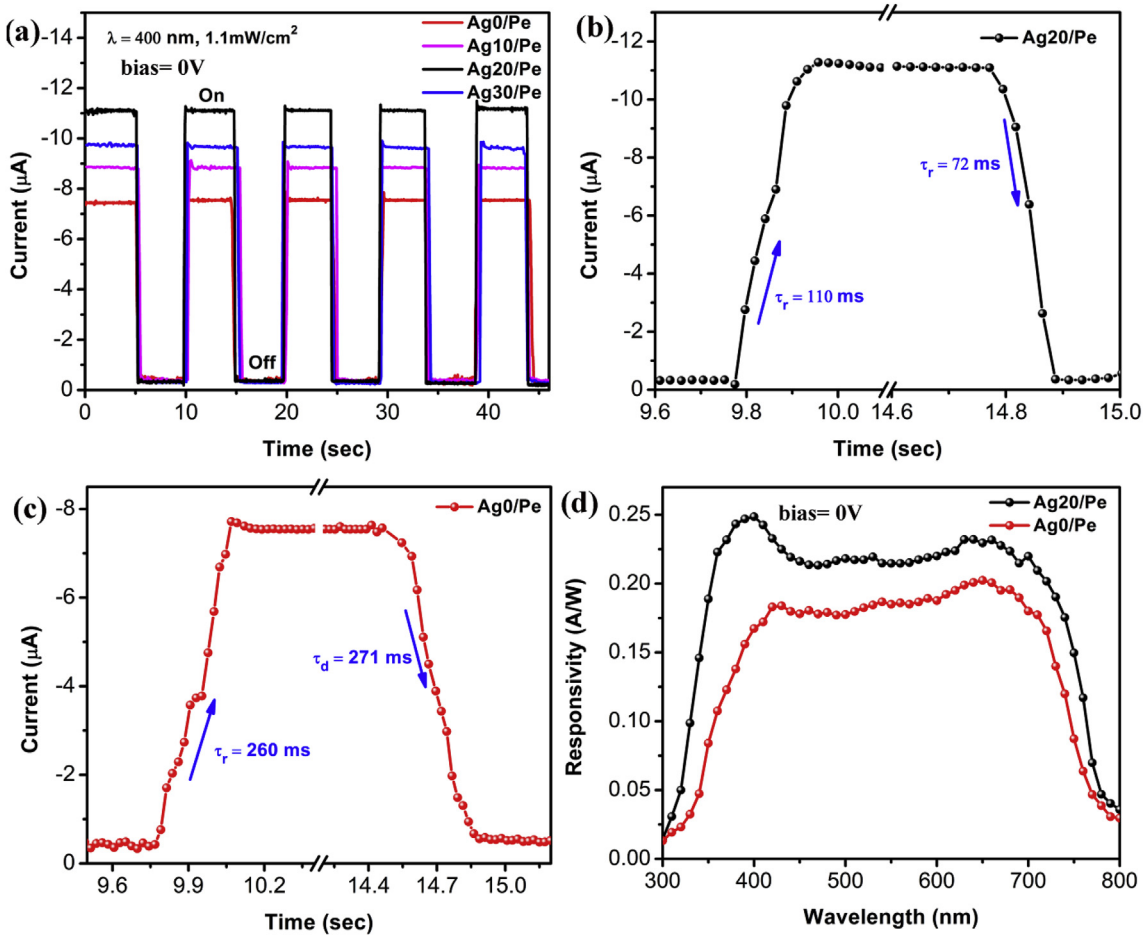

Fig. 4. (a) Time-dependent photocurrent response (at 400 nm light of intensity 1.1 mW/cm^2) of the perovskite photodetector under zero bias without and with Ag NPs at different concentrations. (b, c) An enlarged view of growth and decay profiles of photocurrent of the devices with Ag NPs (Ag20) and without Ag NPs (Ag0), respectively. The growth and decay time constants are indicated with arrows. (d) The wavelength-dependent responsivity of pristine and hybrid photodetector without any external bias.

maximum current value down to 10%, respectively [35]. The time constant of PC growth is found to be τ_r = 110 ms and 260 ms for Ag20 and Ag0 devices, respectively at zero applied bias under 1.1 mW/cm^2 incident light intensity of 400 nm. It is clear that the device with Ag NPs responds faster with higher current gain than the pristine one. This is due to the enhanced plasmonic absorbance and better charge transport by the Ag NPs. Similarly, the time constant (τ_d) of the PC decay is found to be 72 ms and 271 ms, respectively for Ag20 and Ag0 device at zero applied bias under 1.1 mW/cm^2 incident light intensity of 400 nm.

Note that with the addition of PCBM ETL, the PC increased for both the pristine and hybrid device due to higher carrier transport to the electrodes. The time-dependent PC response of Ag0 and Ag20 device with PCBM ETL under zero bias is shown in Fig. S5(a) (supporting information) with ON/OFF intervals of 5 s with 400 nm incident light. Although the devices with organic ETL layer shows higher photocurrent and improved responsivity than the ETL free device, as shown in S5 (supporting information), such organic layers are not desirable considering the cost, toxicity and stability issues [2]. Note that the enhancement of the PC of the hybrid device with ETL is much less that of the ETL free device. In particular, under low bias (0.5 V) the PC is increased to nearly double and responsivity is increased by ~58% in the ETL free hybrid device (see Fig. 5). This may be due to the higher and faster transport of the photogenerated carriers to the electrodes in the presence of the ETL layer. Thus, the plasmonic effect of the Ag NPs is dominant in the device without ETL. Therefore, contributing to the efforts towards ETL-free photodetectors, we have focused on the performance of the ETL free self-biased devices functionalized with plasmonic Ag NPs. Cyclic stability study reveals a very small decrease in the PC after 28 cycles as shown in Fig. S6 (supporting information), and it implies high stability of the device even under ambient air with high humidity.

The spectral responsivity (R_λ) is an important parameter to estimate the performance of the photodetector which indicates how efficiently the detector responds to an optical signal. The responsivity is given by the equation [7,8].

$$R_\lambda = \frac{I_{ph}}{PS} \tag{3}$$

Where I_{Ph} is the photocurrent, P is the incident light power density, and S is the effective illuminated area (4 mm^2). Fig. 4(d) shows the spectral responsivity of the pristine and hybrid photodetectors without any external bias. The self-biased ETL-free $CH_3NH_3PbI_3$ pristine photodetector shows responsivity of 0.18–0.20 AW^{-1} in the region 400–720 nm, which is comparable/higher to the reported transport layer free self-biased Pe photodetector [16,36,37]. From 4(d), it is clear that the responsivity of the hybrid device increased significantly with the incorporation of plasmonic Ag NPs. The hybrid photodetector shows improved responsivity of 0.20–0.25 AW^{-1} in the wavelength region 400–720 nm with the highest responsivity 0.25 AW^{-1} at 400 nm. The enhanced responsivity of the hybrid device in the entire visible region is attributed to the improved carrier extraction and transport by the plasmonic Ag NPs. From Fig. 4(d), it is evident that the enhancement of responsivity in the near UV region (330–500 nm) in the hybrid device is much higher than the visible region. It is believed that the enhanced optical

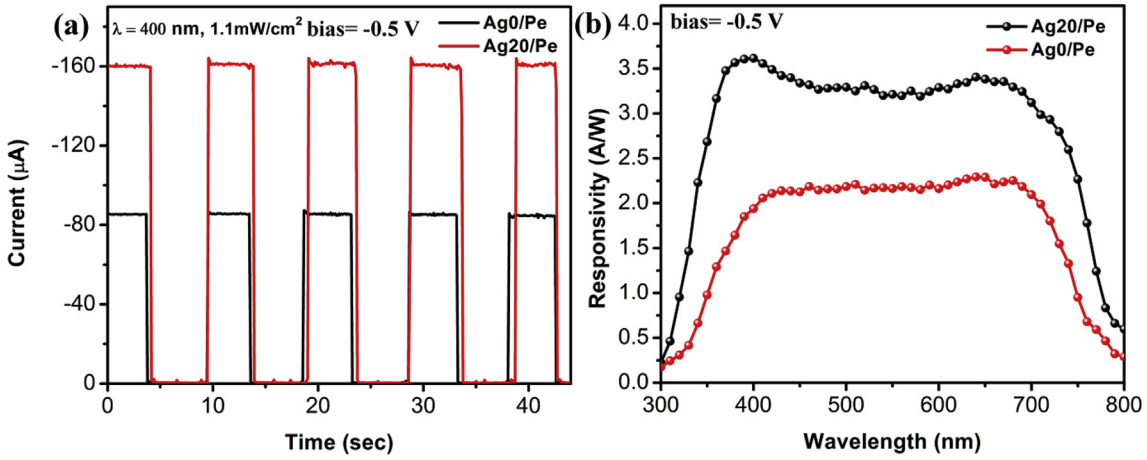

Fig. 5. (a) Time-dependent photocurrent response of the perovskite photodetector under −0.5 V applied bias without (Ag0/Pe) and with Ag NPs (Ag20/Pe) at 400 nm light of intensity 1.1 mW/cm^2. (b) The wavelength-dependent responsivity of pristine and hybrid photodetector at −0.5 V applied bias.

Table 1
Comparison of the characteristic parameters of the self-powered photodetectors reported in the literature with that of the present work.

Device structure	Rise time, decay time	Responsivity [AW^{-1}]	Reference
FTO/PEDOT:PSS + Ag NPs/$CH_3NH_3PbI_3$/Al	110 ms, 72 ms	0.25	This study
C60/$CH_3NH_3PbI_3$/GaN	450 ms, 630 ms	0.20	[19]
C/TiO_2/$CH_3NH_3PbI_3$/CuO/Cu_2O/Cu	200 ms, 200 ms	0.56	[24]
ITO/Au NRs/$CH_3NH_3PbI_3$/Spiro-MeOTAD//MoO_3/Ag	–	0.44	[16]
Au/P(VDF-TrFE)/$CH_3NH_3PbI_3$/Au	92 μs, 193 μs	0.02	[23]
FTO/TiO_2/graphene/$CH_3NH_3PbI_3$/PTAA	5 ms, 5 ms	0.38	[28]

absorption by the Ag NPs causes the higher enhancement in the responsivity in the near UV region, while the enhanced carrier extraction and transport by the plasmonic NPs result in the enhanced responsivity in the entire visible-NIR region. Fig. S5(b) (supporting information) shows the wavelength dependent responsivity of the pristine and hybrid photodetector with PCBM electron transporting layer. Note that with ETL the enhancement of responsivity in the hybrid device is much smaller than the pristine device. Thus the plasmonic effect of the Ag NPs is dominant in the device without ETL and hence it is advantageous to incorporate the plasmonic NPs in the ETL free photodetectors for improved performance. The comaprison of different parameters of our device with previously reported self-powered perovskite photodetectors is shown in Table 1. Our plasmonic-perovskite hybrid photodetector shows comparable performance with the reported self-powered perovskite devices. Note that our device is fabricated entirely in an ambient atmosphere with the modified perovskite deposition method and it is devoid of the ETL layer. Thus, the performance comparison suggests that the present approach is suitable for practical device fabrication. Next, we measure the specific detectivity of the pristine and hybrid photodetectors. The specific detectivity (D^*) of the photodetector represents the capability of detecting low-level light signals, taking into account the contributions of the photocurrent and dark current. D^* can then be expressed by the equation [8,38].

$$D^* = \frac{R_\lambda}{(2qJ_d)^{\frac{1}{2}}} \quad (4)$$

Where R_λ is the spectral responsivity, q is the elementary electron charge, J_d is the dark current density. The pristine device shows a maximum detectivity of 1.04×10^{11} Jones, while the hybrid device reveals a higher detectivity of 1.53×10^{11} Jones as shown in Fig. S7 (Supporting Information).

In order to evaluate the performance of the photodetector under very low bias condition, we measured the PC response under a reverse bias of 0.5 V. Fig. 5(a) shows the time-dependent PC response curves under 0.5 V with 400 nm incident light of intensity 1.1 mW/cm^2. Interestingly, the PC increased significantly with such a small reverse bias (0.5 V), though the enhancement factor is much higher for the plasmonic photodetector case. Note that the applied reverse bias in the device enables easier photogenerated carrier transport to the electrodes resulting in the superior device performance. Fig. 5(b) depicts the spectral responsivity of Ag0 and Ag20 devices with 0.5 V reverse bias. The hybrid device shows the highest responsivity of 3.61 A/W, while the pristine device shows the highest responsivity of 2.28 A/W at 0.5 V bias. This implies a 58% improvement in the responsivity of the hybrid device made with plasmonic Ag nanoparticles, which is significant.

Fig. 6(a) represents the current density versus voltage (J-V) plot of the pristine and hybrid photodetector in dark and light illumination (400 nm light with 1.1 mW/cm^2), respectively. The dark current of the hybrid device is similar to that of the pristine device because of the large Schottky barrier at the contact between Pe and Al electrode [16]. With illumination, the hybrid Ag20 photodetector shows a significantly higher PC than the Ag0 (pristine). Under reverse bias, band bending in the Pe layer close to Al electrode reduces the Schottky junction thickness and enables the injection of carriers into the Pe, leading to dramatic increase in the PC in both pristine and hybrid devices. From Fig. 6(a), it is clear that even at 0 V, there is a significant PC in both the pristine and hybrid device. This is owing to the fact that there exists a built-in electric field in the heterojunction device, which can force the photogenerated carriers in the absorber to be separated and collected by different electrodes. Thus, this photodetector can be self-powered and works at 0 V bias.

The dependence of photocurrent density on the incident light intensity is shown in Fig. 6(b). A 405 nm laser is used for this measurement. The pristine and hybrid devices show linear increment in current density with the incident light intensity in the range of 0.14–15.64 mW/cm^2 at 0 V bias. It is clear that at a higher light intensity, the enhancement in PC for the hybrid device is higher than that of the pristine device. This may be due to the enhanced hot electron

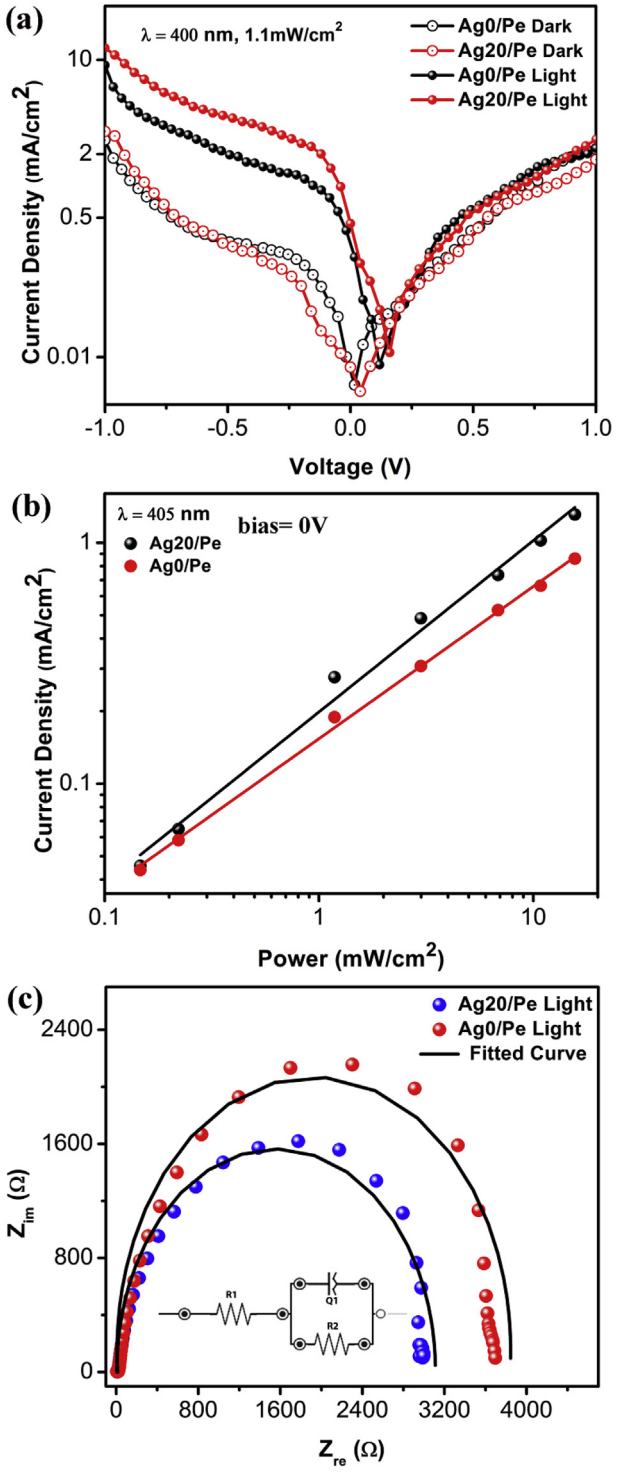

Fig. 6. (a) The J–V characteristics of the photodetector with and without Ag NPs in the dark and under illumination. (b) Intensity-dependent photocurrents of pure and hybrid photodetectors under zero bias at 405 nm incident light with corresponding linear fitting. (c) Impedance spectra of photodetector without and with Ag NPs under illumination at 400 nm of intensity 1.1 mW/cm^2. The inset shows the equivalent circuit diagram.

generation, efficient charge extraction and transport by the plasmonic Ag NPs at a higher intensity [16].

Organometal halide perovskite, especially, $CH_3NH_3PbI_3$ usually shows very poor stability in the ambient atmosphere and degrades very fast in humid condition, i.e., in presence of water and oxygen molecules [2]. We have measured the stability of our plasmonic-perovskite device. Fig. S8 (supporting information) shows the normalized photocurrent with time exposed in ambient air up to 50 h with humidity ~60%. Note that we have measured our device without any encapsulation or protection. Compared to the Organometal halide perovskite, all inorganic perovskite photodetector shows better stability [39,40]. But the performance is much lower compared to the $CH_3NH_3PbI_3$ based devices. The Ag NPs can also react with organometal halide perovskites. Note that we added Ag NPs dispersion with PEDOT:PSS and sonicated thoroughly to make homogeneous dispersion. So, we expect that most of the Ag NPs are embedded in PEDOT:PSS layer or coated with PEDOT:PSS, which are separated from perovskite interface. However, the possibility of some fraction of Ag NPs being present at the interface with perovskite cannot be ruled out and it may react with the perovskite and eventually degrade the device performance.

To analyze the capacitance and resistance components of the multilayered pristine and hybrid devices, the impedance characteristics were measured under illumination at 400 nm at intensity 1.1 mW/cm^2 by impedance spectroscopy as shown in Fig. 6(c) [41]. The electrochemical impedance plots were fitted to a circuit shown in the equivalent circuit diagram in the inset of Fig. 6(c), where the series resistance R1 is connected to a parallel R–C circuit [41]. However, the capacitor is modeled by a constant phase element which is better to reflect the capacitive factors in a thin film photodetector device. The Levenberg-Marquardt method as built into the fitting software PSTrace 5 was used for the fitting. Under illumination, series resistance R1 was determined to be 14.32 Ω for the pristine device and 6.19 Ω for the hybrid device. This series resistance denotes the carrier transfer resistance and therefore is inversely proportional to the efficiency of the hole transfer across the heterojunction [42]. Thus, the carrier transfer efficiency is enhanced (doubled) in the presence of Ag NPs in the hybrid device (see Fig. 6(c)).

The comparison of the work function of Ag0 and Ag20 layers was estimated by KPFM. Fig. 7(a) and (c) shows the AFM topography of Ag0 and Ag20 layer, while Fig. 7(b) and (d) shows the surface potential image of Ag0 and Ag20, respectively. The Ag0 (bare PEDOT:PSS film) shows the surface potential in the range 0–0.244 V, while Ag20 shows values in the range 0–0.197 V. As the KPFM image indicated a uniform distribution of the surface potential across multiple spots that we imaged, we can assume that the surface potential of pristine and PEDOT:PSS film with Ag NPs is uniform on a macroscopic scale. Thus 0.047 V decrease in surface potential of the Ag20 film corresponds to its higher work function of 47 meV than that of the Ag0 film [43,44]. The change of the work function and band alignment of the hybrid device is shown in Fig. 8 [25,41,45]. The dotted line is the work function of Ag0, while the solid line corresponds to the work function of Ag20. Thus the increase in the work function of Ag20 brings it closer to that of the Pe film, and it helps to reduce the energy barrier between the FTO/Pe interface [46]. This enables a superior carrier transport resulting in improved photodetection performance of Ag20. Therefore, the enhanced performance of the ETL-free hybrid Pe is attributed to (a) plasmon-enhanced higher optical absorption and hot electron generation, and (b) improved charge extraction and transport in PEDOT:PSS film with Ag NPs by favorable band alignment. It is quite likely that hot electrons contribute significantly to the improved performance of the ETL-free hybrid photodetector demonstrated here. Further optimization of the plasmonic layer may lead to improved device performance.

4. Conclusion

In conclusion, we have demonstrated the superior performance of the ETL free self-biased Pe photodetector by integrating the plasmonic Ag NPs in the HTL layer. A novel N_2 gas assisted fast crystallization method is used for the perovskite layer deposition to form uniform Pe layer compared to the conventional deposition method in ambient condition. The zero-bias responsivity of the hybrid device is enhanced by ~45% compared to the pristine device, with a peak responsivity of

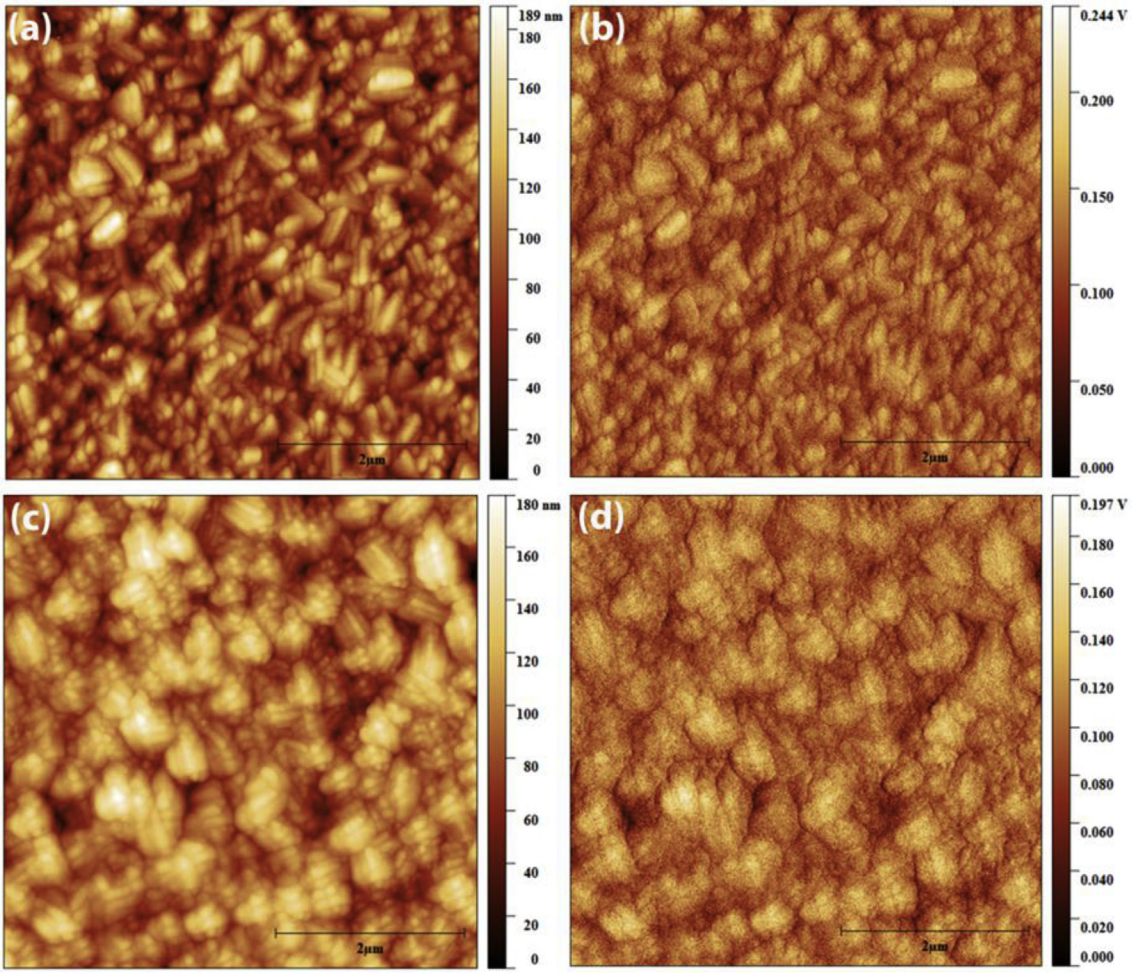

Fig. 7. (a, c) AFM surface topography images of FTO/Ag0 and FTO/Ag20 film, respectively. (b, d) The corresponding KPFM surface potential images.

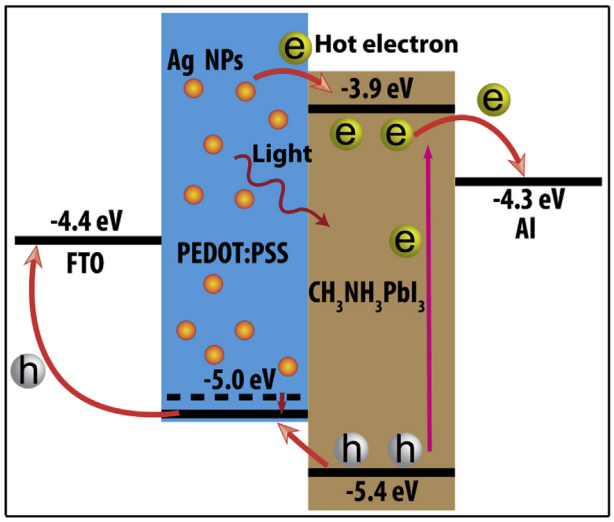

Fig. 8. Schematic of the band diagram illustrating the charge separation and transport processes in ETL-free hybrid photodetector under zero bias.

0.25 AW^{-1}, while the detectivity is enhanced from 1.04×10^{11} Jones (pristine device) to 1.53×10^{11} Jones (hybrid device). The hybrid device also shows about 3 times faster photoresponse as compared to the pristine device. Under small reverse bias (0.5 V), the hybrid device exhibited a peak responsivity of 3.61 A/W, which is significantly higher than the Si-based commercial photodetectors. The improved performance of the hybrid photodetector is attributed to plasmon-enhanced optical absorption, as well as improvement in charge extraction and transport by Ag NPs, which are evidenced by the steady-state and time-resolved photoluminescence analysis. Impedance analysis of the devices shows the reduced carrier transfer resistance of the hybrid device, which results in superior transport of photogenerated charge carriers. Kelvin probe force microscopy analysis revealed an increase in the work function of PEDOT:PSS film with Ag NPs resulting in a favorable band alignment with reduced energy barrier at the interface to enable a superior carrier transport resulting in improved photodetection performance for the hybrid device. Our results open up the possibility of fabrication of air processed low-cost ETL free plasmonic perovskite photodetectors with high performance.

Acknowledgment

We acknowledge the financial support from Meity (Grant No. 5(9)/2012-NANO(VOL-II)) and DST (DST/INSPIRE/04/2016/000881) for carrying out this work. Central Instrument Facility, I.I.T. Guwahati is acknowledged for the FESEM and TRPL facilities.

Appendix A. Supplementary data

Supplementary data to this article can be found online at https://doi.org/10.1016/j.orgel.2019.05.021.

References

[1] S.I. Seok, M. Grätzel, N.-G. Park, Methodologies toward highly efficient perovskite solar cells, Small 14 (2018) 1704177.
[2] Y. Liyan, T.B. Alexander, G.L. David, W. Tao, Recent progress and challenges of organometal halide perovskite solar cells, Rep. Prog. Phys. 79 (2016) 026501.
[3] J. Ghosh, R. Ghosh, P.K. Giri, Mesoporous Si nanowire templated controlled fabrication of organometal halide perovskite nanoparticles with high photoluminescence quantum yield for light-emitting applications, ACS Appl. Nano Materials 1 (2018) 1551–1562.
[4] J. Ghosh, R. Ghosh, P.K. Giri, Strong cathodoluminescence and fast photoresponse from embedded CH3NH3PbBr3 nanoparticles exhibiting high ambient stability, ACS Appl. Mater. Interfaces 11 (2019) 14917–14931.
[5] H. Wang, D.H. Kim, Perovskite-based photodetectors: materials and devices, Chem. Soc. Rev. 46 (2017) 5204–5236.
[6] C. Bao, W. Zhu, J. Yang, F. Li, S. Gu, Y. Wang, T. Yu, J. Zhu, Y. Zhou, Z. Zou, Highly flexible self-powered organolead trihalide perovskite photodetectors with gold nanowire networks as transparent electrodes, ACS Appl. Mater. Interfaces 8 (2016) 23868–23875.
[7] Y. Wang, Q. Song, T. Lin, Y. Fu, X. Sun, B. Chu, F. Jin, H. Zhao, W. Li, Z. Su, Y. Li, Improved performance of CH3NH3PbI3 based photodetector with a MoO3 interface layer, Org. Electron. 49 (2017) 355–359.
[8] L. Dou, Y. Yang, J. You, Z. Hong, W.-H. Chang, G. Li, Y. Yang, Solution-processed hybrid perovskite photodetectors with high detectivity, Nat. Commun. 5 (2014) 5404.
[9] A.Z. Ayan, H. Md Azimul, Y. Jun, M.E.-Z. Ahmed, L. Kwang Jae, D. Ibrahim, F.M. Omar, B. Derya, M.B. Osman, Reduced ion migration and enhanced photoresponse in cuboid crystals of methylammonium lead iodide perovskite, J. Phys. D 52 (2019) 054001.
[10] A. Waleed, M.M. Tavakoli, L. Gu, S. Hussain, D. Zhang, S. Poddar, Z. Wang, R. Zhang, Z. Fan, All inorganic cesium lead iodide perovskite nanowires with stabilized cubic phase at room temperature and nanowire array-based photodetectors, Nano Lett. 17 (2017) 4951–4957.
[11] X. Wang, M. Li, B. Zhang, H. Wang, Y. Zhao, B. Wang, Recent progress in organometal halide perovskite photodetectors, Org. Electron. 52 (2018) 172–183.
[12] W.-L. Xu, M.-S. Niu, X.-Y. Yang, J. Xiao, H.-C. Yuan, C. Xiong, X.-T. Hao, Carbon nanotubes as the effective charge transport pathways for planar perovskite photodetector, Org. Electron. 59 (2018) 156–163.
[13] S. Li, S. Tong, J. Yang, H. Xia, C. Zhang, C. Zhang, J. Shen, S. Xiao, J. He, Y. Gao, B. Yang, J.-Q. Meng, High-performance formamidinium-based perovskite photodetectors fabricated via doctor-blading deposition in ambient condition, Org. Electron. 47 (2017) 102–107.
[14] Y. Fu, Q. Song, T. Lin, Y. Wang, X. Sun, Z. Su, B. Chu, F. Jin, H. Zhao, W. Li, C.S. Lee, High performance photomultiplication perovskite photodetectors with PC60BM and NPB as the interlayers, Org. Electron. 51 (2017) 200–206.
[15] G. Konstantatos, E.H. Sargent, Nanostructured materials for photon detection, Nat. Nanotechnol. 5 (2010) 391.
[16] H. Wang, J.W. Lim, L.N. Quan, K. Chung, Y.J. Jang, Y. Ma, D.H. Kim, Perovskite–gold nanorod hybrid photodetector with high responsivity and low driving voltage, Adv. Opt. Mater 6 (2018) 1701397.
[17] Y. Berencén, S. Prucnal, F. Liu, I. Skorupa, R. Hübner, L. Rebohle, S. Zhou, H. Schneider, M. Helm, W. Skorupa, Room-temperature short-wavelength infrared Si photodetector, Sci. Rep. 7 (2017) 43688.
[18] R. Khokhra, B. Bharti, H.-N. Lee, R. Kumar, Visible and UV photo-detection in ZnO nanostructured thin films via simple tuning of solution method, Sci. Rep. 7 (2017) 15032.
[19] H. Zhou, J. Mei, M. Xue, Z. Song, H. Wang, High-stability, self-powered perovskite photodetector based on a CH3NH3PbI3/GaN heterojunction with C60 as an electron transport layer, J. Phys. Chem. C 121 (2017) 21541–21545.
[20] L. Pengfei, B.N. Shivananju, Z. Yupeng, L. Shaojuan, B. Qiaoliang, High performance photodetector based on 2D CH 3 NH 3 PbI 3 perovskite nanosheets, J. Phys. D 50 (2017) 094002.
[21] K. Jong Min, S. Dong Hee, C. Suk-Ho, Highly-flexible perovskite photodiodes employing doped multilayer-graphene transparent conductive electrodes, Nanotechnology 29 (2018) 425203.
[22] H. Wu, Z. Su, F. Jin, H. Zhao, W. Li, B. Chu, Improved performance of perovskite photodetectors based on a solution-processed CH3NH3PbI3/SnO2 heterojunction, Org. Electron. 57 (2018) 206–210.
[23] F. Cao, W. Tian, L. Meng, M. Wang, L. Li, Ultrahigh-performance flexible and self-powered photodetectors with ferroelectric P(VDF-TrFE)/Perovskite bulk heterojunction, Adv. Funct. Mater. 29 (2019) 1808415.
[24] H. Sun, W. Tian, F. Cao, J. Xiong, L. Li, Ultrahigh-performance self-powered flexible double-twisted fibrous broadband perovskite photodetector, Adv. Mater. 30 (2018) 1706986.
[25] C. Xie, F. Yan, Enhanced performance of perovskite/organic-semiconductor hybrid heterojunction photodetectors with the electron trapping effects, J. Mater. Chem. C 6 (2018) 1338–1342.
[26] B.R. Sutherland, A.K. Johnston, A.H. Ip, J. Xu, V. Adinolfi, P. Kanjanaboos, E.H. Sargent, Sensitive, fast, and stable perovskite photodetectors exploiting interface engineering, ACS Photonics 2 (2015) 1117–1123.
[27] K. Mahmood, S. Sarwar, M.T. Mehran, Current status of electron transport layers in perovskite solar cells: materials and properties, RSC Adv. 7 (2017) 17044–17062.
[28] J. Li, S. Yuan, G. Tang, G. Li, D. Liu, J. Li, X. Hu, Y. Liu, J. Li, Z. Yang, S.F. Liu, Z. Liu, F. Gao, F. Yan, High-performance, self-powered photodetectors based on perovskite and graphene, ACS Appl. Mater. Interfaces 9 (2017) 42779–42787.
[29] J. Ghosh, P.K. Giri, Effect of plasmonic metal nanoparticles on the performance of air processed inverted perovskite solar cells, AIP Conf. Proc. 2082 (2019) 050004.
[30] B. Du, W. Yang, Q. Jiang, H. Shan, D. Luo, B. Li, W. Tang, F. Lin, B. Shen, Q. Gong, X. Zhu, R. Zhu, Z. Fang, Plasmonic-functionalized broadband perovskite photodetector, Adv. Opt. Mater 6 (2018) 1701271.
[31] S. Yang, Y.C. Zheng, Y. Hou, X. Chen, Y. Chen, Y. Wang, H. Zhao, H.G. Yang, Formation mechanism of freestanding CH3NH3PbI3 functional crystals: in situ transformation vs dissolution–crystallization, Chem. Mater. 26 (2014) 6705–6710.
[32] R. Ghosh, J. Ghosh, R. Das, L.P.L. Mawlong, K.K. Paul, P.K. Giri, Multifunctional Ag nanoparticle decorated Si nanowires for sensing, photocatalysis and light emission applications, J. Colloid Interface Sci. 532 (2018) 464–473.
[33] J. Ghosh, R. Ghosh, P.K. Giri, Tuning the visible photoluminescence in Al doped ZnO thin film and its application in label-free glucose detection, Sensor. Actuator. B Chem. 254 (2018) 681–689.
[34] A. Sharma, B. Bhattacharyya, A.K. Srivastava, T.D. Senguttuvan, S. Husale, High performance broadband photodetector using fabricated nanowires of bismuth selenide, Sci. Rep. 6 (2016) 19138.
[35] S. Tong, H. Wu, C. Zhang, S. Li, C. Wang, J. Shen, S. Xiao, J. He, J. Yang, J. Sun, Y. Gao, Large-area and high-performance CH3NH3PbI3 perovskite photodetectors fabricated via doctor blading in ambient condition, Org. Electron. 49 (2017) 347–354.
[36] Y. Wang, T. Zhang, P. Zhang, D. Liu, L. Ji, H. Chen, Z.D. Chen, J. Wu, S. Li, Solution processed PCBM-CH3NH3PbI3 heterojunction photodetectors with enhanced performance and stability, Org. Electron. 57 (2018) 263–268.
[37] L. Li, C. Wang, C. Wang, S. Tong, Y. Zhao, H. Xia, J. Shi, J. Shen, H. Xie, X. Liu, D. Niu, J. Yang, H. Huang, S. Xiao, J. He, Y. Gao, Interfacial electronic structures of MoOx/mixed perovskite photodetector, Org. Electron. 65 (2019) 162–169.
[38] F. Tang, Q. Chen, L. Chen, F. Ye, J. Cai, L. Chen, Mixture interlayer for high performance organic-inorganic perovskite photodetectors, Appl. Phys. Lett. 109 (2016) 123301.
[39] M. Gong, R. Sakidja, R. Goul, D. Ewing, M. Casper, A. Stramel, A. Elliot, J.Z. Wu, High-performance all-inorganic CsPbCl3 perovskite nanocrystal photodetectors with superior stability, ACS Nano 13 (2019) 1772–1783.
[40] M. Xue, H. Zhou, G. Ma, L. Yang, Z. Song, J. Zhang, H. Wang, Investigation of the stability for self-powered CsPbBr3 perovskite photodetector with an all-inorganic structure, Sol. Energy Mater. Sol. Cells 187 (2018) 69–75.
[41] C.H. Ji, K.T. Kim, S.Y. Oh, High-detectivity perovskite-based photodetector using a Zr-doped TiOx cathode interlayer, RSC Adv. 8 (2018) 8302–8309.
[42] Z. Liang, P. Zeng, P. Liu, C. Zhao, W. Xie, W. Mai, Interface engineering to boost photoresponse performance of self-powered, broad-bandwidth PEDOT:PSS/Si heterojunction photodetector, ACS Appl. Mater. Interfaces 8 (2016) 19158–19167.
[43] P. Wang, D. Tanaka, S. Ryuzaki, S. Araki, K. Okamoto, K. Tamada, Silver nanoparticles with tunable work functions, Appl. Phys. Lett. 107 (2015) 151601.
[44] S. Intu, B.R. Mehta, Optical properties and band alignments in ZnTe nanoparticles/MoS 2 layer hetero-interface using SE and KPFM studies, Nanotechnology 28 (2017) 445701.
[45] P. Chen, Z. Xiong, X. Wu, M. Shao, Y. Meng, Z.-h. Xiong, C. Gao, Nearly 100% efficiency enhancement of CH3NH3PbBr3 perovskite light-emitting diodes by utilizing plasmonic Au nanoparticles, J. Phys. Chem. Lett. 8 (2017) 3961–3969.
[46] Z. Zhao, Q. Wu, F. Xia, X. Chen, Y. Liu, W. Zhang, J. Zhu, S. Dai, S. Yang, Improving the conductivity of PEDOT:PSS hole transport layer in polymer solar cells via copper(II) bromide salt doping, ACS Appl. Mater. Interfaces 7 (2015) 1439–1448.